Supplement of Atmos. Chem. Phys., 18, 2653–2667, 2018
https://doi.org/10.5194/acp-18-2653-2018-supplement

Atmospheric Chemistry and Physics
Open Access
EGU

Supplement of

Size distribution and coating thickness of black carbon from the Canadian oil sands operations

Yuan Cheng et al.

Correspondence to: Shao-Meng Li (shao-meng.li@canada.ca)

Table S1. A summary of rBC size distribution parameters for the 14 emission flights, including MMD (mass median diameter; in nm), $Width_{mass}$ (mass distribution width; dimensionless), NMD (number median diameter; in nm), and $Width_{number}$ (number distribution width; dimensionless).

Date (flight ID)	MMD	$Width_{mass}$	NMD	$Width_{number}$
14 August, 2013 (F_8/14)	153.75 ± 0.64	0.71 ± 0.01	76.18 ± 0.64	0.67 ± 0.01
15 August, 2013 (F_8/15)	144.82 ± 0.54	0.74 ± 0.01	66.99 ± 0.44	0.71 ± 0.01
17 August, 2013 (F_8/17)	145.70 ± 1.57	0.72 ± 0.02	66.61 ± 1.33	0.73 ± 0.02
19 August, 2013 (F_8/19)	141.82 ± 0.58	0.75 ± 0.01	61.12 ± 0.65	0.75 ± 0.01
20 August, 2013 (F_8/20)	134.46 ± 0.99	0.74 ± 0.02	62.18 ± 0.80	0.72 ± 0.01
21 August, 2013 (F_8/21)	136.19 ± 0.67	0.70 ± 0.01	63.99 ± 0.69	0.72 ± 0.01
22 August, 2013 (F_8/22)	141.98 ± 0.98	0.70 ± 0.01	64.35 ± 1.16	0.74 ± 0.01
24 August, 2013 (F_8/24)	135.46 ± 0.94	0.74 ± 0.02	63.14 ± 0.56	0.71 ± 0.01
26 August, 2013 (F_8/26)	135.02 ± 0.37	0.61 ± 0.01	78.38 ± 0.54	0.61 ± 0.01
28 August, 2013 (F_8/28)	138.82 ± 0.71	0.74 ± 0.01	63.77 ± 0.41	0.72 ± 0.00
29 August, 2013 (F_8/29)	134.00 ± 0.46	0.70 ± 0.01	64.65 ± 0.48	0.70 ± 0.01
2 September, 2013 (F_9/2)	135.78 ± 2.04	0.72 ± 0.03	63.71 ± 1.13	0.71 ± 0.01
3 September, 2013 (F_9/3)	137.53 ± 0.93	0.76 ± 0.02	64.64 ± 0.70	0.70 ± 0.01
6 September, 2013 (F_9/6)	135.01 ± 0.77	0.71 ± 0.01	66.00 ± 0.71	0.69 ± 0.01

Table S2. A summary of rBC size distribution parameters for the 3 transformation flights. Results from successive flight screens are shown separately for each flight.

Flight and screen ID	MMD	$Width_{mass}$	NMD	$Width_{number}$
4 September, 2013 (F_9/4)				
Screen #1	140.87 ± 0.43	0.70 ± 0.01	69.07 ± 0.36	0.69 ± 0.00
Screen #2	141.13 ± 0.88	0.71 ± 0.01	71.59 ± 0.62	0.67 ± 0.01
Screen #3	147.47 ± 1.45	0.74 ± 0.02	71.11 ± 0.95	0.69 ± 0.01
Screen #4	146.97 ± 2.71	0.76 ± 0.04	71.11 ± 0.89	0.68 ± 0.01
Screen #5	142.42 ± 0.60	0.68 ± 0.01	72.00 ± 0.47	0.67 ± 0.01
19 August, 2013 (F_8/19)				
Screen #1	139.76 ± 1.67	0.76 ± 0.03	58.21 ± 2.26	0.77 ± 0.03
Screen #2	139.33 ± 1.78	0.74 ± 0.03	63.33 ± 2.04	0.73 ± 0.02
Screen #3	145.12 ± 1.57	0.79 ± 0.02	59.33 ± 2.29	0.78 ± 0.03
5 September, 2013 (F_9/5)				
Screen #1	149.85 ± 2.46	0.74 ± 0.03	70.88 ± 1.23	0.70 ± 0.02
Screen #2	148.79 ± 1.19	0.67 ± 0.02	72.67 ± 0.92	0.70 ± 0.01
Screen #3	151.62 ± 1.54	0.71 ± 0.02	73.48 ± 1.51	0.70 ± 0.02

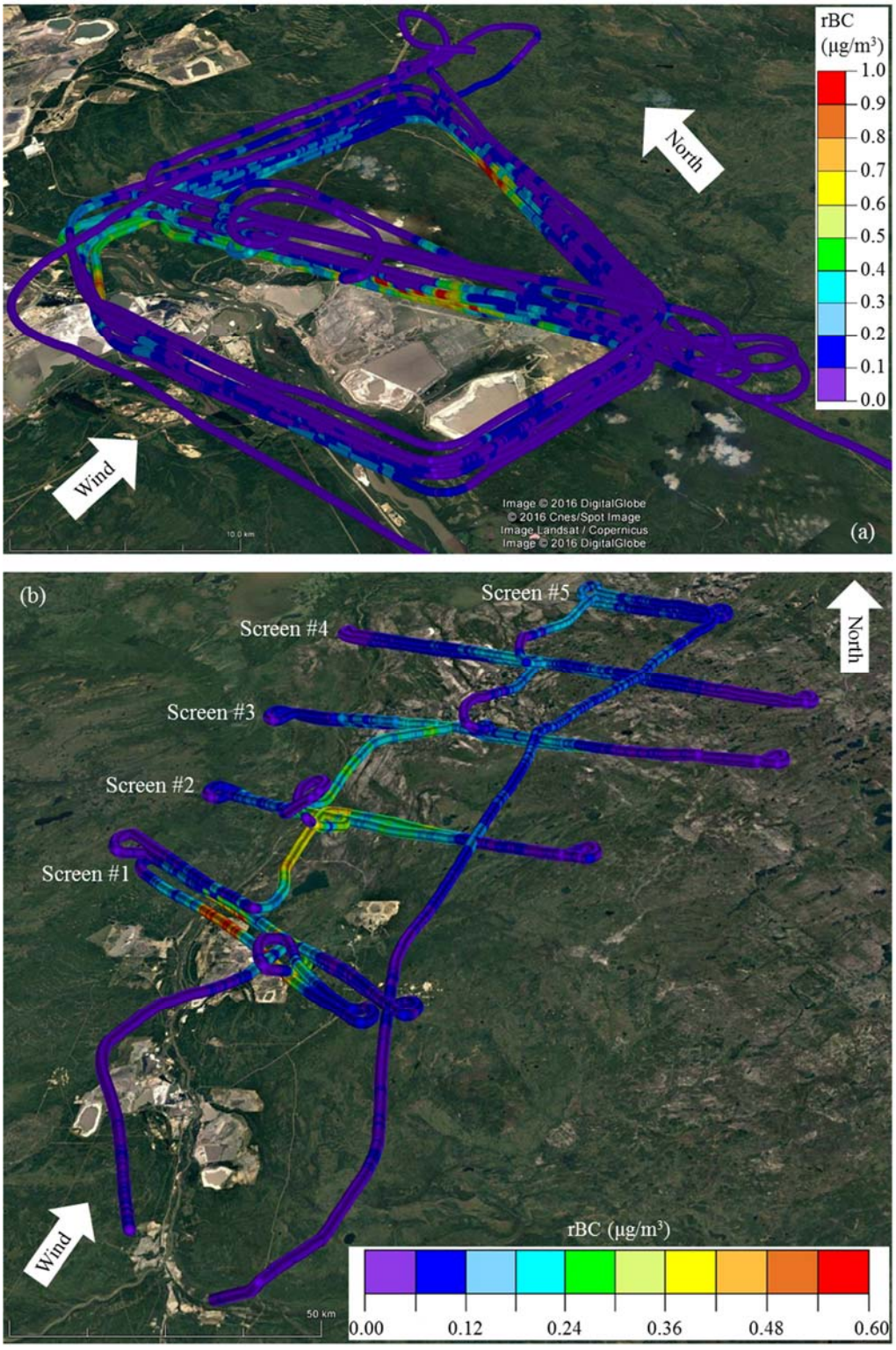

Figure S1. Composite Google Earth images showing flight tracks (colored by rBC mass concentration) for F_8/28 (a) and F_9/4 (b).

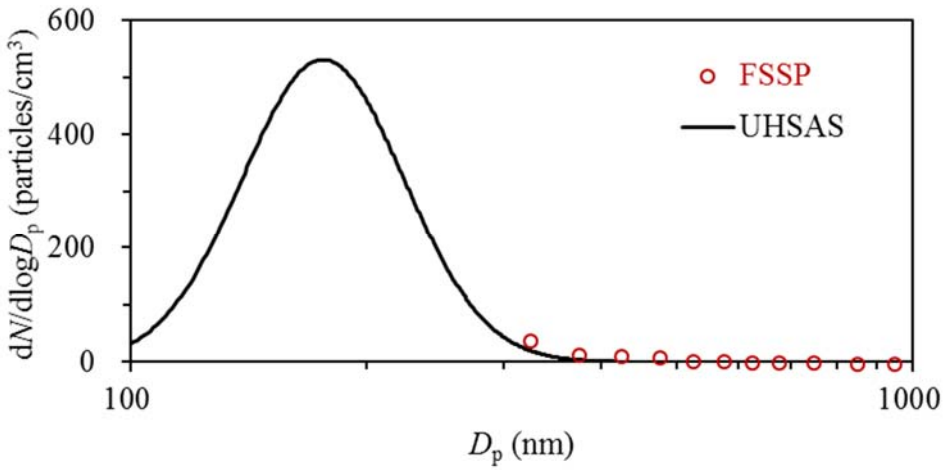

Figure S2. Comparison of particle number size distributions derived from wing-mounted FSSP and inboard UHSAS based on results from segments of the transformation flight conducted on August 19, 2013. These segments were flown at different downwind distances from the oil sands source area, along level flight tracks at multiple altitudes. FSSP and UHSAS measure optical sizes for particles in the diameter ranges of 0.3 to 20 μm and 0.06 to 1.0 μm, respectively, with an overlapping detection range of 0.3 to 1.0 μm. Measurement results from FSSP are shown only for the overlapping size range. For UHSAS, the measurement results exhibited a bimodal distribution for the flight segments investigated; only the mode at relatively large sizes, which is characteristic of the accumulation mode, is shown for comparison with FSSP. Although FSSP and UHSAS can be compared only at the trailing edge of the UHSAS size distribution, an agreement is observed between these two instruments in terms of both particle numbers and their size distributions. This agreement suggests that in the aerosol inlet and sampling line, both the particle loss and the evaporation loss from the particles should be minimal for the < 1.0 μm size range.

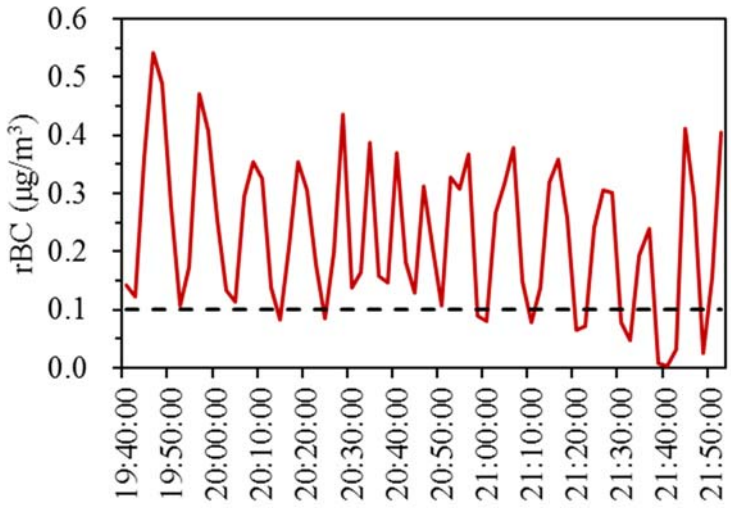

Figure S3. Temporal variation of 2-min averaged rBC mass concentration during F_8/26. The dashed line indicates an rBC concentration of 0.1 μg/m^3 which can be used to distinguish the typical in- and out-of-plume conditions for this flight.

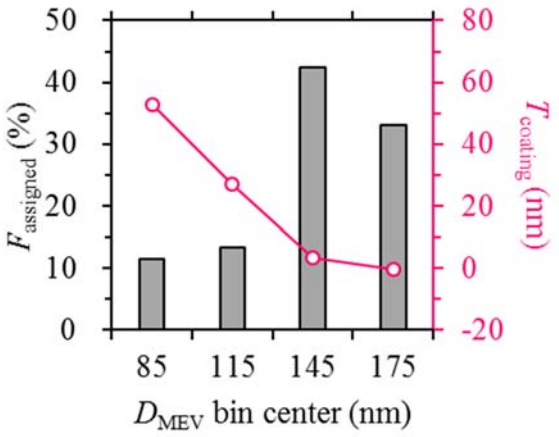

Figure S4. Dependences of coating thickness ($T_{coating}$) and the fraction of rBC cores that can be assigned a coating thickness ($F_{assigned}$, in %) on rBC core size (D_{MEV}) for the emission flight F_9/3. Refer to the caption of Figure 11 in the main manuscript for more details.

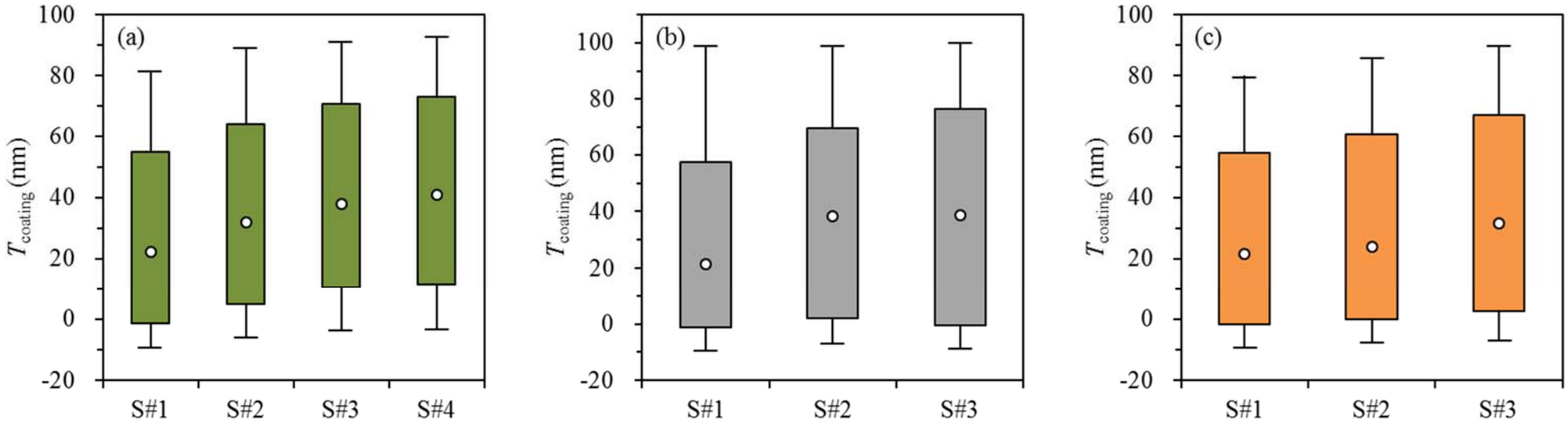

Figure S5. Evolutions of in-plume coating thickness ($T_{coating}$) for rBC cores in the D_{MEV} range of 130−160 nm during the transformation flights **(a)** F_9/4, **(b)** F_8/19 and **(c)** F_9/5. The counts of the 130−160 nm rBC cores that can be assigned a coating thickness are ~ 2450−3600, 300−400, and 700−1600 for successive flight screens of F_9/4, F_8/19 and F_9/5, respectively. $F_{assigned}$ are ~ 35−45%, 30−35%, and 30−45% for the 130−160 nm rBC cores observed during F_9/4, F_8/19 and F_9/5, respectively.

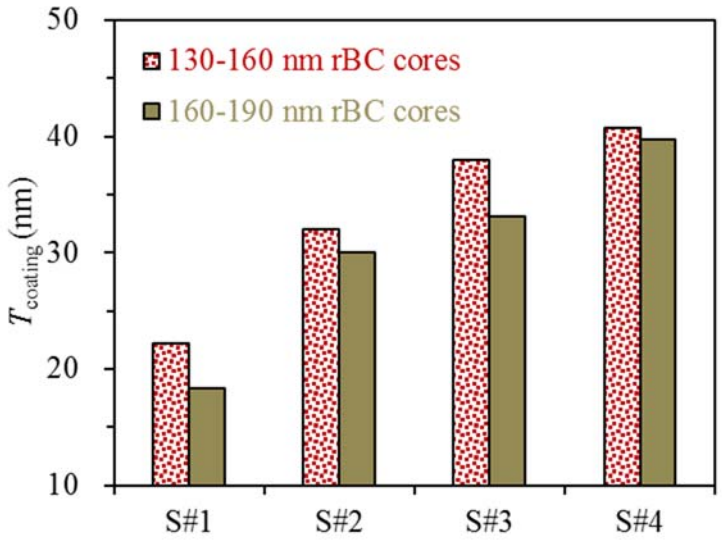

Figure S6. Comparison of coating thicknesses ($T_{coating}$) for in-plume rBC cores in two different D_{MEV} ranges (i.e., 130−160 nm and 160−190 nm) during the transformation flight F_9/4. Results from successive flight screens are shown separately. Coating thicknesses determined for 160−190 nm rBC cores are smaller than those for 130−160 nm rBC cores, which can be attributed to the limitation that the detection range of $T_{coating}$ is rBC D_{MEV} dependent. Evolutions of $T_{coating}$ exhibit the same pattern for rBC cores in the two different D_{MEV} ranges. However, both the count of rBC cores that can be assigned a coating thickness and the fraction of rBC cores that can be assigned a coating thickness are higher for the D_{MEV} range of 130−160 nm. Therefore, 130−160 nm rBC cores are used in the main manuscript for discussions on $T_{coating}$.